Applied Catalysis B: Environmental 337 (2023) 122982

Contents lists available at ScienceDirect

Applied Catalysis B: Environmental

journal homepage: www.elsevier.com/locate/apcatb

A one-pot synthesis of high-density biofuels through bifunctional mesoporous zeolite-encapsulated Pd catalysts

Qiang Deng [a,*], Honggen Peng [b,*], Zhenzhen Yang [c], Tao Wang [c], Jun Wang [a], Zheling Zeng [a], Sheng Dai [c,*]

[a] School of Chemical and Chemical Engineering, Nanchang University, No. 999 Xuefu Avenue, Nanchang 330031, PR China
[b] School of Resources and Environment, Nanchang University, No. 999 Xuefu Avenue, Nanchang 330031, PR China
[c] Chemical Sciences Division, Oak Ridge National Laboratory, Oak Ridge, TN 37830, USA

ARTICLE INFO

Keywords:
Pd@meso-ZSM-5
Cyclic ketones
Bicyclic alkanes
Aldol condensation
Hydrodeoxygenation

ABSTRACT

Developing a powerful bifunctional catalyst for tandem reactions is essential to the future carbon neutrality by reducing the energy consumption in chemical industries. Herein, mesoporous zeolite-encapsulated palladium (Pd) nanoparticles (Pd@meso-ZSM-5) synthesized via emulsification-demulsification followed by a dry-gel transformation method were demonstrated to have a remarkable catalytic performance for a one-pot multiple tandem reaction of cyclic ketones (cyclopentanone, cyclohexanone) to bicyclic alkanes (bicyclopentane, bicyclohexane). Compared with supported catalysts (Pd/meso-ZSM-5) and microporous zeolite-encapsulated catalysts (Pd@ZSM-5) with a primary product of monocyclic alkane (cyclopentane, cyclohexane), Pd@meso-ZSM-5 shows much higher catalytic efficiency for the bicyclic alkanes synthesis, which was previously unattainable in the conventional two-step synthesis route. Controlled experiments and detailed characterizations show that mesoporosity provides sufficient space for the generation and diffusion of large molecular intermediates, and the intimate acid-Pd interface promotes the conversion of intermediates. This work proposes a design strategy for a mesoporous zeolite-encapsulated metal catalyst, which efficiently provides cooperative acid-hydrogenation catalysis.

1. Introduction

High-density jet fuel, composed of cyclic hydrocarbons, is an indispensable propellent in some specific volume-limited aircraft (such as rockets, warplanes, and missiles). They possess a greater volume calorific value than conventional jet fuel and can extend the flight range and increase the loading capacity of aircraft [1,2]. Currently, their synthesis is dominated by the conversion of petroleum-based cyclic hydrocarbons (such as cyclopentadiene). To mitigate the excessive depletion of fossil resources and decrease emissions of carbon dioxide, lignocellulose offers an attractive alternative, as it is a widely available biomass resource [3]. Lignocellulose is readily transformed into furan-based platform compounds, such as furfural, 5-hydroxymethylfurfural, and 2-methylfuran, which provide an excellent entry point for upgrading [4,5]. Typically, as has been widely reported, some $C_{10–17}$ linear and branched alkanes can be generated via an aldol cross-condensation of furfurals with acetone (e.g., furfural and 5-hydroxymethylfurfural) or alkylation of 2-methylfuran with acetone followed by a hydrodeoxygenation reaction [6,7]. However, linear alkanes possess a low density (<0.79 g/mL). To increase biofuel density, some biobased cyclic ketones (e.g., cyclopentanone and cyclohexanone) have been introduced as feedstocks to replace acetone. For example, some monocyclic alkanes (density of 0.81–0.84 g/mL) were obtained via an aldol cross-condensation of furan aldehydes with cyclic ketones or alkylation of 2-methylfuran with cyclic ketones [8–10]. Some bicyclic alkanes (density of 0.88–0.90 g/mL) were synthesized by aldol self-condensation of cyclic ketones [11–15]. Obviously, bicyclic alkanes with a higher density and volumetric calorific value are more desirable.

The current two-step synthesis of bicyclic alkanes from cyclic ketones suffers from some issues. First, for the condensation of cyclic ketones, although numerous acid catalysts (such as ion exchange resins, acid-treated clays, and metal oxide) and base catalysts (such as sodium hydroxide, lithium perchlorate, and triethylamine) exhibit considerable catalytic activity, the selectivity of bicyclic alkanes precursors (mono-condensed products) is unsatisfactory due to the further condensation of mono-condensed products with cyclic ketones [11–19].

* Corresponding authors.
E-mail addresses: dengqiang@ncu.edu.cn (Q. Deng), penghonggen@ncu.edu.cn (H. Peng), dais@ornl.gov (S. Dai).

https://doi.org/10.1016/j.apcatb.2023.122982
Received 4 April 2023; Received in revised form 6 June 2023; Accepted 8 June 2023
Available online 10 June 2023

Some microporous zeolites (such as ZSM-5 and Hβ) have been attempted to suppress the generation of macromolecular di-condensed byproducts, but their pore sizes are too small to show inactivity [20]. Second, for the hydrodeoxygenation step, some acidic zeolites have been used as supports or physical mixtures (such as Pd/Hβ, Pd/ZSM-5, Pd/C + ZSM-5) to provide acidic sites for dehydration reactions [11–15]. However, the small pore size of zeolite and spatially separated metal and acid sites strongly limit the mass transport rate of intermediates. The catalytic activities are always weak, and harsh reaction conditions (such as elevated reaction temperatures of 180–250 °C) are needed. Third, the separation and purification of mono-condensed products in the condensation reaction mixture would make the technological process complicated and impractical. In modern organic synthesis, the direct one-pot strategy has received particular interest to integrate multiple sequential steps under the same reaction conditions [21–23]. In this regard, the design of zeolite-confined metal nanoparticles is significant to reduce the physical distance between acid sites and metal sites, thereby boosting the synergistic function of acid catalysis and hydrogenation catalysis.

Multiple synthetic methods of zeolite-encapsulated metal nanoparticles with abundant acid-metal interfaces have been widely reported. (1) Iglesia's group pioneered a mercaptosilane-assisted hydrothermal synthesis based on the strong coordination of mercapto groups with the noble metal [24]. (2) Then, Iglesia and Yu's group established ligand-protected hydrothermal synthesis by the stabilization of ligand-containing metal precursors under hydrothermal conditions [25–28]. (3) Xiao and Corma's group proposed a method of encapsulation in zeolite by seed-directed growth and interzeolite transformation using metal-containing zeolite seeds as precursors [29,30]. In addition, a solvent-free crystallization method was also developed by using metal-encapsulated silicon dioxide (SiO_2) as a precursor [31–33]. Recently, Xu's group synthesized cationic polymer-protected and steam-assisted crystallization synthesis via the electrostatic interaction of polydiallyldimethylammonium chloride (PDDA) with anionic metal precursors and silicate or aluminosilicate sources [34–36]. At present, these catalysts are mainly microporous. Xu and Li's group showed that platinum (Pt) encapsulated in ZSM-5 (Pt@ZSM-5) outperforms the corresponding Pt-supported sample in the one-pot conversion of biomass derivatives to small molecular products, such as tandem condensation and hydrogenation of furfural with acetone to hydrogenated C_8 products [34], tandem hydrogenation and hydrogenolysis of furfural to 2-methylfuran [35], tandem hydrolysis and hydrodeoxygenation of furfural to valeric acids [36]. However, for the transformation of cyclopentanone to bicyclic alkanes, microporous Pt@ZSM-5 can only generate cyclopentane and hinder the production of macromolecular intermediates [37].

Against this backdrop, we envisaged that zeolites containing abundant mesoporous and acid-metal interfaces can simultaneously promote aldol condensation and their subsequent hydrodeoxygenation steps. Herein, a series of mesoporous ZSM-5-encapsulated Pd nanoparticles (Pd@meso-ZSM-5) were fabricated with different acid amounts based on the emulsification-demulsification and dry-gel transformation method. To the best of our knowledge, this is the first report on the integration of mesoporosity and an acid-Pd interface for ZSM-5-based bifunctional catalysts. The acid amount is well governed by the amount of aluminum (Al) sources. The catalysts possess a specific surface area of 400–500 m^2/g and mesoporous sizes of 2 and 20 nm. In the direct transformation of cyclic ketones, the microporous counterpart (Pd@ZSM-5) and supported counterpart (Pd/meso-ZSM-5) show a primary product of monocyclic alkane, whereas Pd@meso-ZSM-5 possesses bicyclic alkane yields above 85%. Furthermore, the composite catalyst can be stabilized for at least 4 recycles. The catalyst system opened a door toward facile and efficient synthesis of high-density biofuel.

2. Experimental

2.1. Synthesis of Pd@meso-ZSM-5

The details of reagents are provided in the Supporting information. Mesoporous ZSM-5 encapsulated Pd nanoparticle (Pd@meso-ZSM-5) was synthesized by emulsification-demulsification and a subsequent dry-conversion method. First, amorphous aluminosilicate shell encapsulated Pd core (Pd@Al_2O_3-SiO_2) was prepared via a continuous emulsification-demulsification method. Brifely, 5.3 mL of tetraamminepalladium dinitrate ($Pd(NH_3)_4(NO_3)_2$) aqueous solution (0.7 wt%) was rapidly added to 960.0 mL of polyethylene glycol mono-4-nonyl phenyl ether (NP-5) cyclohexane solution (5.3 wt%) at 30 °C and stirred for 12 h to form the microemulsion system. Then, 4.3 mL of ammonia solution (28 wt%$NH_3{\cdot}H_2O$), 4.7 g of tetraethoxysilane and a certain amount of aluminum isopropoxide (0.09, 0.06 g, the corresponding molar ratio of SiO_2/Al_2O_3 =50, 75) were added, and the mixture was stirred for 48 h at 30 °C. Subsequently, 200 mL of methanol was added for demulsification for 0.5 h, and Pd@Al_2O_3-SiO_2 was collected by centrifugation separation and dried in a vacuum oven at 60 °C overnight. Subsequently, Pd@meso-ZSM-5 was synthesized by the conversion of amorphous Al_2O_3-SiO_2 shell over Pd@Al_2O_3-SiO_2 to ZSM-5 through a dry-gel conversion method. Briefly, 1 g of the resultant dry gel and 5 mL of tetrapropylammonium hydroxide aqueous solution (25 wt%) was ground for 0.5 h, moved into a 10 mL tank, and put into a 100 mL tank in a stainless-steel autoclave, and 5 mL of water was added to the external tank. Then, the autoclave was kept in an oven for pre-crystallization at 80 °C for 48 h, and the temperature was raised to 120 °C for crystallization for 24 h. The solid was transformed to H-form via a twice ion-exchange process with 10 mL aqueous solution ammonium nitrate (8.0 wt%NH_4NO_3) at 80 °C for 2 h. Finally, the resultant Pd@meso-ZSM-5 was obtained after drying at 150 °C, calcination in air at 550 °C for 4 h, and reduction at 300 °C for 2 h under a 10% H_2/Ar atmosphere. The catalyst characterization analyses are detailed in the Supporting information.

2.2. Catalytic reactions

The tandem aldol condensation and hydrodeoxygenation reactions were carried out in a 50 mL batch autoclave (NST25-P5-T3-SS1-R, Anhui Chem-n Instrument Co., Ltd) equipped with mechanical stirring. Typically, 1 mmol of cyclopentanone or cyclohexanone, 0.04 g of catalyst, and 25 mL of cyclohexane were added into the reactor under the string. Before the reaction, the air in the reactor was replaced with hydrogen several times. Then, the mixture was heated to 160 °C under hydrogen pressure, and periodically sampled with 0.5 mL after reaching the target reaction time. If not mentioned, the hydrogen pressure was 1.0 MPa. Subsequently, 10 μL of N,N-dimethylamide was used as an internal standard substance. The reaction mixture was qualitatively analyzed by an Agilent 6890 N GC/5973 MS detector and quantitatively analyzed by a Trace 1300 gas chromatograph equipped with a TG-WAXMS capillary column (30 m × 0.32 mm). The carbon loss during the reaction was attributed to the formation of humins. The CPO conversion, BCP yield and selectivity were calculated as follows.

$$\text{CPO conversion}(\%) = \frac{C_{CPO,0} - C_{CPO}}{C_{CPO,0}} * 100\%$$

$$\text{BCP yield}(\%) = \frac{2C_{BCP}}{C_{CPO,0}} * 100\%$$

$$\text{BCP selectivity}(\%) = \frac{\text{BCP yield}}{\text{CPO conversion}} * 100\%$$

3. Results and discussion

3.1. Synthesis and characterization

Mesoporous Pd@meso-ZSM-5 is obtained via an emulsification-demulsification and subsequent dry-gel transformation method with a lower crystallization temperature and a lesser template (Fig. 1A). For comparison, microporous Pd@ZSM-5 with encapsulated structures was synthesized by traditional hydrothermal synthesis according to our previous work with some modifications using ligand-containing Pd $(NH_3)_4(NO_3)_2$ as a Pd source [38]. The X-ray diffraction (XRD) patterns of Pd@ZSM-5 and Pd@meso-ZSM-5 confirmed the high crystallinity of MFI phase zeolites (Fig. 1B), indicating that the introduction of guest Pd nanoparticles does not affect the preparation of the ZSM-5 host. Inductively coupled plasma-optical emission spectrometry (ICP-OES) indicates that all catalysts possess an approximate Pd content of 1 wt% and Si/Al ratio of 50 (Table 1). The characteristic peaks of Pd nanoparticles are under-detected, which indicates that the encapsulated sample possesses ultrahigh dispersion of Pd nanoparticles during the calcination and reduction process at high temperatures. Transmission electron microscope (TEM) images of these Pd-encapsulated samples exhibit no aggregates on the host surface; instead, they are all encapsulated with a size of 3–8 nm (Fig. 1C, 1D, S1). Section tomography over different sections further confirms that the nanoparticles were located within the zeolite crystals (Fig. 1E, S1). TEM image exhibits the lattice spacings of zeolite (0.99 nm, 020 lattice plane) and Pd nanoparticles (0.226 nm, 111 lattice plane) [39–41]. Subsequently, the high-angle annular dark-field scanning TEM (HAADF-STEM) image and elemental mapping of Pd@meso-ZSM-5 show that Pd and Al signals possess synchronous intensities (Fig. S2), demonstrating that Pd nanoparticles and Al atoms are homogeneously dispersed in the host. Moreover, the Pd signal has a much weaker intensity, illustrating the structure of the Pd

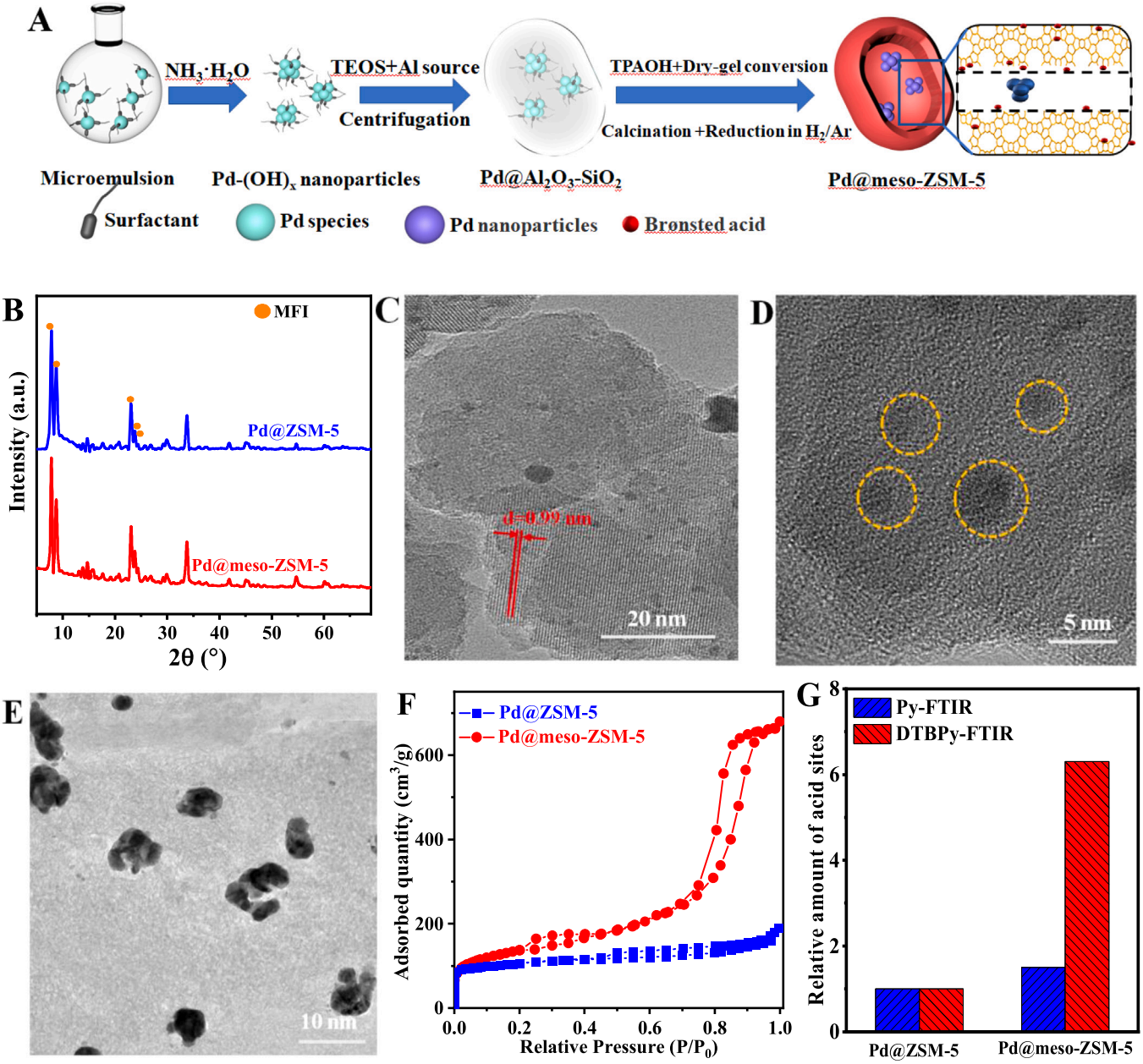

Fig. 1. (A) Synthesis process of Pd@meso-ZSM-5; (B) XRD patterns of catalysts; (C), (D) TEM and (E) section tomography images of Pd@meso-ZSM-5; (F) N_2 adsorption/desorption isotherms of catalysts; (G) relative amount of accessible acid sites determined by pyridine absorption and 2,6-di-tert-butylpyridine adsorption (based on Pd@ZSM-5).

Table 1
Physicochemical properties of catalysts. a detected by ICP-OES; b detected by XPS.

Catalyst	Pd content[a] (wt %)	Pd content[b] (at %)	SiO_2/Al_2O_3 ratio	S_{BET} ($m^2 \cdot g^{-1}$)	V_{total} ($cm^3 \cdot g^{-1}$)	V_{micro} ($cm^3 \cdot g^{-1}$)	Acid amount (mmol/g)	Dispersity (%)
Pd@ZSM-5	0.97	0.04	52.0	354.4	0.24	0.22	0.40	31
Pd@meso-ZSM-5	0.90	0.05	48.4	482.1	1.07	0.21	0.39	33
Pd/meso-ZSM-5	1.04	0.44	45.2	456.8	1.01	0.21	0.35	13

core and zeolite shell. The Pd 3d spectra of the X-ray photoelectron spectra (XPS) can only be deconvoluted into two peaks at 335.0 ($3d_{5/2}$ peak of Pd^0) and 340.2 eV ($3d_{3/2}$ peak of Pd^0) (Fig. S3) [42], without the signal of Pd^{2+} appear. Meanwhile, XPS indicates the Pd 3d atomic percentages are only 0.04–0.05, indicating that the Pd nanoparticles are mainly encapsulated inside the zeolite [34,43]. The Pd dispersity was also confirmed by H_2-O_2 titration based on the H_2 consumption of completely oxidized samples, which follows the similar dispersity of 31–33% (Fig. S4, Table 1) [44]. Dispersed Pd nanoparticles are beneficial for H_2 activation, which is a significant step for this reaction process.

The N_2 adsorption isotherms of Pd@ZSM-5 are type I curves with a plateau starting at 0.1 P/P_0 and ending at 0.9 P/P_0, corresponding to micropores of 0.55 nm (Fig. 1F). In addition to Type I isotherms, Pd@meso-ZSM-5 possess a type IV isotherm with two hysteresis loops of 0.2–0.4 and 0.7–0.9 P/P_0, corresponding to two mesopores of approximately 2 nm and 20 nm, which are attributed to the existence of intracrystalline mesopores caused by a structure-directing agent (NP-5) in the Al_2O_3-SiO_2 dry gel and the generation of intercrystallite mesopores during the dry-gel conversion procedure, respectively (Fig. S5). As summarized in Table 1, the specific surface area and pore volume of Pd@ZSM-5 are 354.4 $m^2 \cdot g^{-1}$ and 0.24 $cm^3 \cdot g^{-1}$, respectively. For Pd@meso-ZSM-5, the specific area and volume are significantly increased to 482.1 $m^2 \cdot g^{-1}$ and 1.07 $cm^3 \cdot g^{-1}$, presenting well-reserved microporosity and generated mesoporosity. Hierarchical structures with connected micropores and mesopores possess readily open active sites and improved conductivity for large molecules.

The ^{27}Al magic-angle spinning nuclear magnetic resonance (^{27}Al MAS NMR) spectra show that the Al^{3+} sites in all catalysts are mainly located in the framework, indexed by a high concentration signal at 53.1 ppm (ascribed to tetrahedral Al^{3+}) and a very weak signal near − 0.7 ppm (ascribed to octahedral Al^{3+}) (Fig. S6) [34–37]. The acid amount was determined by temperature-programmed desorption of ammonia (NH_3-TPD), all the samples exhibit double peaks centered at 163 and 297 °C, corresponding to weak and strong acid sites (Fig. S7). The samples possess a similar acid amount of 0.39–0.40 $mmol \cdot g^{-1}$ due to the similar Si/Al ratio (Table 1). Meanwhile, the acidity was obtained by infrared spectroscopy of adsorbed pyridine (Py-FTIR) and 2, 6-di-tert-butylpyridine (DTBPy-FTIR). In Py-FTIR spectra, the acid amount of Lewis and Brønsted acid sites was calculated by the Emeis equation based on the peak area of chemisorbed pyridine at 1456 and 1542 cm^{-1} (Fig. S8) [45]. The peak area at 1542 cm^{-1} is assigned to pyridinium ion (PyH^+) on Brønsted acidic sites. In agreement with previous works, these ZSM-5-based samples mainly exhibit Brønsted acidity, attributed to Si-O(H)-Al structure [34–37]. In the DTBPy-FTIR, the peaks at 1617 and 1542 cm^{-1} can be ascribed to Brønsted acid sites, and peaks at 1453 cm^{-1} are originated Lewis acid sites [46]. It should be noted that, DTBPy-FTIR shows that Pd@meso-ZSM-5 possess 6.3 times more Brønsted acidic amount than Pd@ZSM-5, whereas the ratio detected by Py-FTIR is only 1.5 times (Fig. 1G). The kinetic diameter of DTBPy (0.80 nm) is larger than the micropore (0.55 nm), and can only be adsorbed on the acid sites located at the external surface. Whereas, the formation of a mesoporous structure in Pd@meso-ZSM-5 is specifically conducive to adsorption of macromolecules [47].

3.2. One-pot conversion of cyclic ketones to bicyclic alkanes

The one-pot transformation of cyclopentanone (CPO) to bicyclopentane (BCP) was first investigated under 160 °C and 1.0 MPa H_2 pressure. As mentioned above, tandem transformation of CPO to bicyclopentane involves aldol condensation of CPO to 2-cyclopentylidene-cyclopentanone (CPECPO) on acid sites, hydrogenation to 2-cyclopentan-cyclopentanol (CPCPL) on Pd nanoparticles, dehydration to cyclopentylidene-cyclopentane (CPECP) on acid sites, and hydrogenation steps on Pd nanoparticles (Fig. 2A). Except for bicyclopentane, some side-product cyclopentane (CP) can be produced via the direct hydrogenation of CPO to cyclopentanol (CPL), dehydration to cyclopentene (CPE), and subsequent hydrogenation step. The di-condensed 2,5-dicyclopentylidene cyclopentanone (DCPECPO) generated by the further condensation of CPECPO and CPO cannot appear. These intermediates and products were proved by gas chromatography-mass spectrometry. Previous reports showed a considerable yield of decalin over Pt@ZSM-5 that derived from two pathways: (1) dehydration of CPL to CPE, dimerization and rearrangement to octahydronaphthalene, and subsequent hydrogenation [37], (2) rearrangement of CPECP to octahydronaphthalene, and subsequent hydrogenation [37]. However, the decalin cannot be detected under our reaction system, which might be due to the stronger hydrogenation ability of Pd than Pt for accelerating the hydrogenation conversion of in situ dehydrated intermediates (cyclopentene, cyclopentylidene-cyclopentane) rather than acid-catalyzed dimerization or rearrangement routes.

Fig. 2B and C show the time-dependent product distribution over Pd@ZSM-5 and Pd@meso-ZSM-5. The reactions show a high carbon balance of more than 98%. For the BCP synthesis, the concentrations of CPECPO and CPECP are trace, which further indicates that their hydrogenation steps are rapid, and the acid-catalyzed aldol condensation of CPO and dehydration of CPCPL steps are relatively slow steps. After 12 h, Pd@ZSM-5 shows considerable activity with an 63.0% conversion of CPO, but a high selectivity of CP (67.6%) and low selectivity of BCP (24.8%) are generated (Fig. 2D). The pore size of Pd@ZSM-5 (0.55 nm) can allow the hydrogenation of CPO (kinetic diameter 0.41 nm) to cyclopentanol (kinetic diameter 0.43 nm) easily, but largely inhibit the production of CPECPO (kinetic diameter 0.68 nm) [48]. In contrast, despite an identical Pd dispersity, Pd@meso-ZSM-5 with hierarchical pore (0.55 nm, 2 nm, and 20 nm) can accommodate the bulky intermediates and products, and CPO tends to be condensed for the synthesis of BCP. It shows both higher CPO conversion of 92.0% and BCP selectivity of 82.3% than Pd@ZSM-5. In addition, by prolongation of the reaction time to 24 h, CPCPL is completely converted and an 87.1% yield of BCP is obtained. The Pd@meso-ZSM-5 shows a superior catalytic performance in terms of catalytic conversion and selectivity than all reported catalysts, especially for traditional noble metal-supported zeolite or the physical mixture of noble metal and zeolite, with unprecedentedly low temperature 160 °C (Table S1) [9,11,12,15,37,49–51]. Even, BCP productivity of the catalytic system is higher than the reported reaction systems using CPECPO as reactant. After the reaction, the spent catalyst was recovered by centrifugation, washed with cyclohexane, and dried before the next run. After 5 runs, a CPO conversion of 99.2% is highly maintained with a BCP selectivity of 85.0% (Fig. 2E). The recycled samples exhibit outstanding stability of the encapsulated zeolite under the reaction conditions (Fig. S9, Table S2). Besides, the

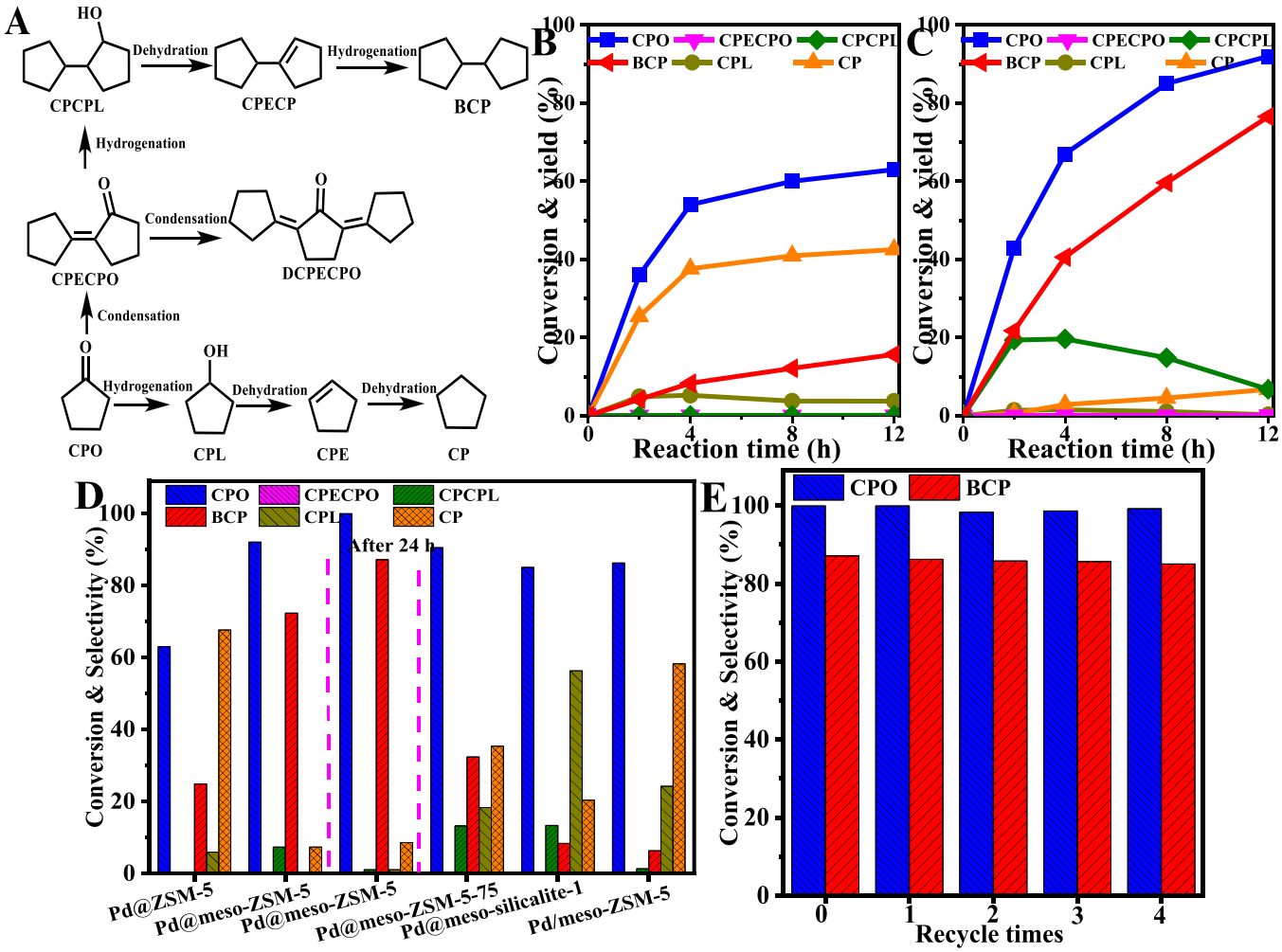

Fig. 2. (A) The main and side reaction pathway of CPO reaction; the temporal evolution of tandem CPO conversion under over (B) Pd@ZSM-5 and (C) Pd@meso-ZSM-5; (D) the catalytic performance of catalysts in CPO reaction; (E) recyclability of Pd@meso-ZSM-5. Reaction condition: CPO (1.0 mmol), catalyst (0.04 g), cyclohexane (25 mL), 160 °C, 1.0 MPa H_2 pressure, 12 h.

recycling performance conducted at a low conversion further proves the stability of Pd@meso-ZSM-5.

Next, these catalysts are also investigated in six-membered ring cyclohexanone (CHO, kinetic diameter 0.51 nm). Biomass-based CHO can be obtained from the hydrogenation of lignin-derived phenols [14, 52]. The synthesis of bicyclohexane (BCH) from CHO proceeds via an identical reaction route of CPO reactions by intermediates 2-cyclohexylidene-cyclohexanone (CHECHO), 2-cyclohexan-cyclohexanol (CHCHL), and (CHECH), supported by the temporal evolution curve of the product distribution (Fig. S10). Meanwhile, a large amount of cyclohexane (CH) is obtained from the direct hydrodeoxygenation of CHO. The catalytic performance still follows same trends: after 12 h, Pd@meso-ZSM-5 shows both higher CHO conversion (99.3% v.s. 69.0%) and BCH selectivity (61.2% v.s. 6.3%) than Pd@ZSM-5 (Fig. 2F). A prolonged reaction time to 24 h can lead to complete conversion of CHO and a 90.1% yield of BCH. Notably, Pd@meso-ZSM-5 still shows distinct advantage in BCH synthesis under the milder reaction conditions (160 °C, 1.0 MPa H_2) (Table S3) [15]. The results demonstrate the universality of the metal-encapsulated mesoporous structure for the tandem aldol condensation and hydrodeoxygenation reaction.

3.3. Understanding of pore size engineering and acidity

To investigate the structure-dependent catalytic performance, kinetic study of CPO aldol condensation was conducted. Based on the initial generation rate of CPECPO-based products (CPECPO, CPCPL, BCP) and CPL-based products (CPL, CP) at 2 h with CPO concentration ranged from 0.01 to 0.05 mol L^{-1}, both CPO aldol condensation and CPO hydrogenation are pseudofirst-order reactions (Fig. S11). Elementary steps for aldol condensation include CPO adsorption, enolate formation, C-C coupling, dehydration, and product desorption. If a bimolecular surface reaction between surface enolate and CPO were rate limiting, the condensation reaction would be second-order kinetic in CPO instead of the observed first order. The pseudofirst-order reaction as expected if CPO adsorption and activation rate determines the condensation step [53,54]. Similarly, the pseudofirst-order reaction of CPO hydrogenation process indicates the CPO adsorption rate determines the hydrogenation step instead of H_2 activation [42]. Correspondingly, the H_2 pressures have little effect on the reactivity, because the H_2 is easily activated and saturated on the Pd surface (Fig. S12). As the hydrogen pressure increases from 1.0 MPa to 4.0 MPa, after 2 h, the CPO condensation and CPO hydrogenation rate only slightly increase from 0.205 to 0.219, and 0.011–0.015 mol L^{-1} g^{-1} h^{-1}, respectively. The condensation kinetic constant follows the order of Pd@ZSM-5 (0.53 g^{-1} h^{-1}) < Pd@meso-ZSM-5 (5.12 g^{-1} h^{-1}) (Fig. 3A). Whereas, the CPO hydrogenation kinetic constant follows a contrasting order of Pd@meso-ZSM-5 (0.25 g^{-1} h^{-1}) < Pd@ZSM-5 (3.74 g^{-1} h^{-1}). Considering that these catalysts possess the same Pd dispersity and acidity, we inferred that the aldol condensation activity is mainly attributed to the pore size engineering. To further confirm the relationship between

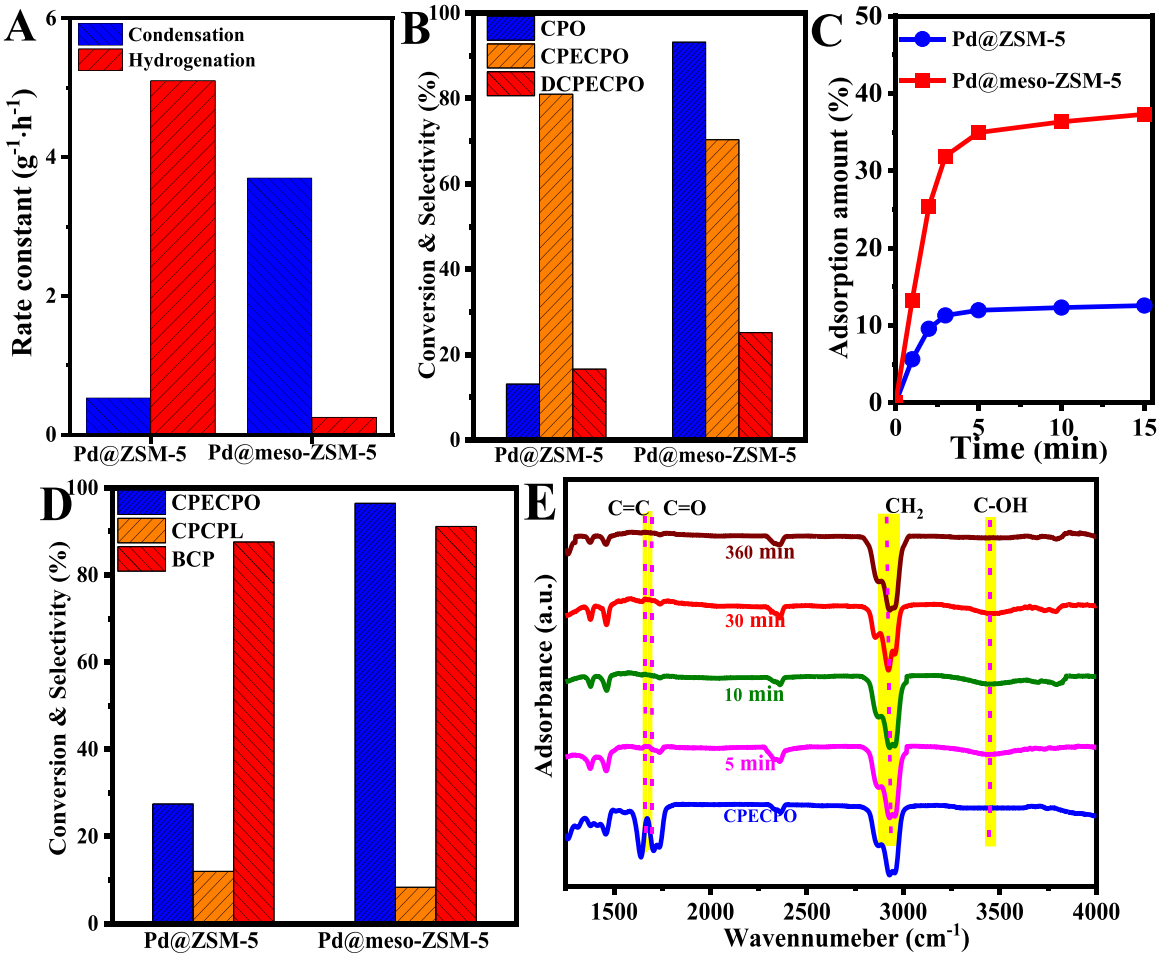

Fig. 3. (A) CPO aldol condensation and hydrogenation kinetic constants over different catalysts; (B) the catalytic performance of catalysts in CPO condensation reaction; (C) adsorption kinetics of CPO over different catalysts; (D) the performance of catalysts in CPECPO hydrodeoxygenation to BCP; (E) DRIFTS spectra of CPECPO over Pd@meso-ZSM-5. Reaction conditions: catalyst (0.04 g), cyclohexane (25 mL), 160 °C, 12 h, (A) CPO (1.0 mmol), 1.0 MPa H_2 pressure, 2 h; (B) CPO (1.0 mmol), 1.0 MPa N_2 pressure; (D) CPECPO (0.5 mmol), 1.0 MPa H_2 pressure. (C) Adsorption condition: CPO (0.1 mmol), Pd@meso-ZSM-5 (0.04 g), cyclohexane (25 mL), 30 °C.

catalytic performance and porous structure, the CPO reaction was carried out under an N_2 atmosphere to completely remove the influence of CPO hydrogenation (Fig. 2A). After 12 h, Pd@meso-ZSM-5 exhibited a much higher CPO conversion (93.2%) than Pd@ZSM-5 (13.1%) (Fig. 3B). The intracrystalline mesopores in meso-ZSM-5 should be key to the higher conversion. To verify the difference in molecular diffusion of microporous and mesoporous zeolite, the adsorption of CPO was measured under 30 °C (Fig. S13). Pd@meso-ZSM-5 has faster adsorption rates and higher adsorption capacities than Pd@ZSM-5 due to the faster diffusion rate of the mesoporous and the higher diffusion accessibility of larger specific surface area (Fig. 3C).

In addition, CPECPO was used as the substrate to replace CPO under the H_2 atmosphere (Fig. S14). The CPECPO conversion and BCP selectivity follow the order of Pd@ZSM-5 (26.5%, 86.6%) <Pd@meso-ZSM-5 (96.5%, 91.1%), as expected since the metal site encapsulated in microporous is difficult to be contacted by macromolecular reactant (Fig. 3D). Meanwhile, the CPECPO hydrogenation rate also follows pseudofirst-order kinetic based on the initial CPECPO concentration, which means CPECPO adsorption rate determines the hydrogenation step [54] (Fig. S15). The hydrogenation kinetic constant follows the order of Pd@ZSM-5 (1.25 $g^{-1}·h^{-1}$) < Pd@meso-ZSM-5 (5.72 $g^{-1}·h^{-1}$). Subsequently, the hydrodeoxygenation mechanism of CPECPO was investigated by liquid phase in situ diffuse reflectance infrared Fourier transform spectroscopy (DRIFTS). With the bubbling of H_2 into the mixture of CPECPO, cyclohexane and Pd@meso-ZSM-5, the intensity of C═C (1701 cm^{-1}) and C═O peaks (1725 cm^{-1}) decreased along with the reaction time (Fig. 3E) [55,56]. Meanwhile, the characteristic peak for -C-OH (3467 cm^{-1}) belonging to CPCPL appeared, and the intensity enhanced along with the reaction proceeded for 10 min, demonstrating the successful hydrogenation over the metal sites. To conduct the further transformation of CPCPL to BCP, the reaction time was extended to 360 min, and the C-OH peak disappeared completely, verifying the hydrodeoxygenation of CPCPL promoted by the acidic sites.

Then, the relationship between catalytic performance and acidity was investigated by manipulating the amount of Al source. Pd@meso-ZSM-5–75 (the atom ratio of Si/Al) and Pd@meso-silicalite-1 (without the addition of Al source) were prepared by a similar dry-gel transformation method. XRD, TEM, ICP-OES, N_2 adsorption isotherms, NH_3-TPD and Py-FTIR show Pd@meso-ZSM-5 and Pd@meso-silicalite-1 possess an identical encapsulated structure, pore properties, acid type distribution with Pd@meso-ZSM-5, except for a lower content of Al elements and acid amount (Fig. S16, Table S4). Our synthesis method has great structure varieties for acid and metal sites. As expected, Pd@meso-ZSM-5–75 and Pd@meso-silicalite-1 show both lower CPO conversion and BCP selectivity than Pd@meso-ZSM-5 (Fig. 2D). More acid sites are conducive to the activation of CPO for the aldol self-condensation.

3.4. Understanding of acid-Pd interface engineering

To investigate the powerful synergy catalysis of Pd-acid interface,

Pd/meso-ZSM-5 with surface-supported metal nanoparticles was prepared by dry-gel transformation and subsequent incipient impregnation method. XRD, TEM, ICP-OES, N_2 adsorption isotherms, NH_3-TPD and Py-FTIR show Pd/meso-ZSM-5 possesses an identical pore property, element distribution, and acidity with Pd@meso-ZSM-5, except for the Pd dispersity and supported structure on the external surface (Fig. S17, Table 1). The much higher Pd3d XPS signal intensity of Pd/meso-ZSM-5 than that of Pd@meso-ZSM-5 suggests that the proportion of the unencapsulated Pd nanoparticles is much smaller in Pd@meso-ZSM-5 than that in Pd/meso-ZSM-5 (Fig. S3). After 12 h, Pd/meso-ZSM-5 shows considerable activity with an 86.2% conversion of CPO, but a high selectivity of CP (58.2%) and low selectivity of BCP (6.3%) are obtained (Fig. 2D, S18). Palladium nanoparticles on the external surface dominate the hydrogenation route of CPO. To illustrate the difference in catalytic results, CPECPO and CPCPL were used as the substrates over Pd/meso-ZSM-5 and Pd@meso-ZSM-5 (Figs. S14, S19). After 2 h, the CPECPO and CPCPL conversion rates follow the same order of Pd@meso-ZSM-5 (0.115, 0.072 mol L^{-1} g^{-1} h^{-1}, respectively) < Pd/meso-ZSM-5 (0.15, 0.074 mol L^{-1} g^{-1} h^{-1}, respectively) (Fig. 4A). Clearly, the CPCPL dehydration step is relatively slow step for the overall reaction. Over Pd/meso-ZSM-5, the formation rate of BCP from CPCPL (0.074 mol L^{-1} g^{-1} h^{-1}) is higher than that from CPECPO (0.024 mol L^{-1} g^{-1} h^{-1}) (Fig. 4B). Generally, the product formation rate from the reactant is slower than that from the intermediate because of the slow diffusion rate between separate acid and hydrogenation sites for additional reaction step [57,58]. However, over Pd@meso-ZSM-5, the BCP formation rate is opposite: CPCPL (0.071 mol L^{-1} g^{-1} h^{-1}) < CPECPO (0.097 mol L^{-1} g^{-1} h^{-1}). The adsorption experiment of CPECPO and CPCPL over Pd@meso-ZSM-5 indicates that CPECPO possesses a higher capacity and faster adsorption rate than CPCPL (Fig. 4C). The intimate hydrogenation and acid sites can remove intermediate diffusion process, and the in situ generated CPCPL on the hydrogenation sites can be quickly dehydrated on the acid sites (Fig. 4D). The efficient cooperation of bifunctional catalysis ensures unprecedented BCP generation efficiency (Table S1).

Moreover, under the N_2 atmosphere, a large amount of DCPECPO can be generated by the further condensation of CPECPO and CPO over the mesoporous samples (Fig. 3B). However, as mentioned above, tricyclic DCPECPO and corresponding derivatives cannot be detected under an H_2 atmosphere. The elimination of the di-condensed product (DCPECPO, kinetic diameter of 0.86 nm) cannot be associated with the spatial control of the mesopore (pore size of 2 and 20 nm) instead of rapid hydrogenation of CPECPO to DCPECPO. Note that the DCPECPO is undesirable because the corresponding tricyclic alkane with a high viscosity and freezing point is not suitable as liquid jet fuels. The trade-off between the conversion of CPO and the selectivity of the CPECPO and its derivatives can be solved by powerful concerted catalysis. This superior proximity of acid and metal sites in encapsulated structures can avoid molecular diffusion between multiple active sites, which efficiently accelerates the hydrogenation conversion of CPECPO and inhibits unwanted further condensation. Therefore, the excellent one-pot conversion catalytic efficiency of Pd@meso-ZSM-5 can be realized by the presence of mesoporosity and acid-metal interfaces.

4. Conclusions

In conclusion, we have developed a series of tunable Pd-acid interface-encapsulated mesoporous zeolites for the tandem aldol condensation of cyclic ketones and subsequent hydrodeoxygenation. Compared with a traditional two-step route, the one-pot conversion is more easily industrialized. They show much a higher yield of bicyclic alkanes from both cyclopentanone and cyclohexanone, than Pd supported

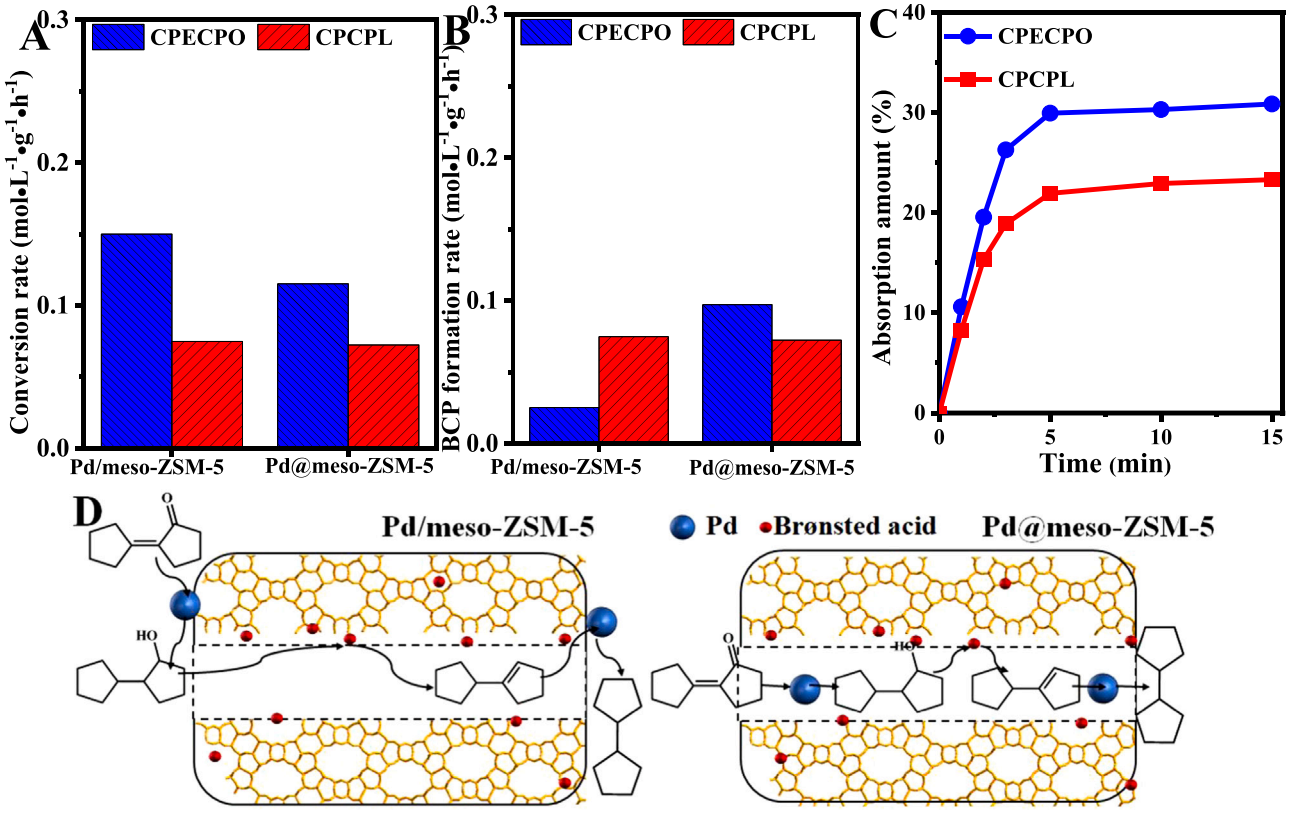

Fig. 4. (A) Conversion rate and (B) BCP formation rate from CPECPO and CPCPL over Pd/meso-ZSM-5 and Pd@meso-ZSM-5. Reaction conditions: CPECPO (0.5 mmol), catalyst (0.04 g), cyclohexane (25 mL), 160 °C, 2 h, 1.0 MPa H_2 pressure. (C) The adsorption kinetics of CPECPO and CPCPL over Pd@meso-ZSM-5. Adsorption conditions: CPECPO/CPCPL (0.05 mmol), Pd@meso-ZSM-5 (0.04 g), cyclohexane (25 mL), 30 °C. (D) Schematic of the CPECPO and CPCPL hydrodeoxygenation over Pd/meso-ZSM-5 and Pd@meso-ZSM-5.

mesoporous zeolite and microporous zeolite-encapsulated Pd counterparts. The mesopore promotes the generation of large molecular intermediates, and the intimate acid-metal interfaces provide the powerful concerted catalysis ability. Furthermore, it maintains stable catalytic activity during the recycled experiments. This is the first report on the integration of mesoporosity and acid-Pd interface for zeolite-based bifunctional high-density biofuel catalysts.

CRediT authorship contribution statement

Qiang Deng: Methodology, Writing-original draft preparation. **Honggen Peng**: Supervision, Software, Validation. **Zhenzhen Yang**: Data curation, Software. **Tao Wang**: Investigation, Conceptualization. **Jun Wang**: Investigation, Conceptualization. **Zheling Zeng**: Investigation. **Sheng Dai**: Supervision, Writing – review & editing.

Declaration of Competing Interest

The authors declare not competing financial interest.

Data Availability

Data will be made available on request.

Acknowledgements

Z.Y., T.W., and S.D. were supported by the US DOE Office of Basic Energy Science. Q.D. and H.P. were supported financially by the National Natural Science Foundation of China (22178158, 52162014, 22065024, 21976078), the Cultivating Project for Academic and Technical Leader of Key Discipline of Jiangxi Province (20212BCJ23038), the Outstanding Youth Science Fund Project of Jiangxi Province (S2022ZRYCL0176), and the Jiangxi Provincial Double Thousand Talents Plan-Youth Program (S2021GDQN0947).

Supporting Information

Some catalyst physicochemical properties and catalytic reaction results, namely, TEM micrographs, EDS mapping, XPS spectra, ^{27}Al MAS NMR spectra, NH_3-TPD, Py-FTIR spectra, DTBPy-FTIR spectra, catalytic kinetics, adsorption experiment, and catalytic effect of H_2 pressure.

Appendix A. Supporting information

Supplementary data associated with this article can be found in the online version at doi:10.1016/j.apcatb.2023.122982.

References

[1] X. Wang, T. Jia, L. Pan, Q. Liu, Y. Fang, J.-J. Zou, X. Zhang, Review on the relationship between liquid aerospace fuel composition and their physicochemical properties, Trans. Tianjin Univ. 27 (2021) 87–109.
[2] J. Nie, T. Jia, L. Pan, X. Zhang, J.-J. Zou, Development of high-energy-density liquid aerospace fuel: a perspective, Trans. Tianjin Univ. 28 (2022) 1–5.
[3] P. Sudarsanam, R. Zhong, V. Sander, S.M. Coman, V.I. Parvulescu, B.F. Sels, Functionalised heterogeneous catalysts for sustainable biomass valorisation, Chem. Soc. Rev. 47 (2018) 8349–8402.
[4] Y. Feng, S. Long, X. Tang, Y. Sun, R. Luque, X. Zeng, L. Lin, Earth-abundant 3d-transition-metal catalysts for lignocellulosic biomass conversion, Chem. Soc. Rev. 50 (2021) 6042–6093.
[5] S. Yang, C. Shi, Z. Shen, L. Pan, Z. Huang, X. Zhang, J.-J. Zou, Conversion of lignin oil and hemicellulose derivative into high-density jet fuel, J. Energy Chem. 77 (2023) 452–460.
[6] G.W. Huber, J.N. Chheda, C.J. Barrett, J.A. Dumesic, Production of liquid alkanes by aqueous-phase processing of biomassderived carbohydrates, Science 308 (2005) 1446–1450.
[7] A. Corma, O. Torre, M. Renz, N. Villandier, Production of high-quality diesel from biomass waste products, Angew. Chem. Int. Ed. 50 (2011) 2375–2378.
[8] X. Zhang, Q. Deng, P. Han, J. Xu, L. Pan, L. W., J.-J. Zou, Hydrophobic mesoporous acidic resin for hydroxyalkylation/alkylation of 2-methylfuran and ketone to high-density biofuel, AIChE J. 63 (2016) 680–688.
[9] Q. Deng, P. Han, J. Xu, J.-J. Zou, L. Wang, X. Zhang, Highly controllable and selective hydroxyalkylation/alkylation of 2-methylfuran with cyclohexanone for synthesis of high-density biofuel, Chem. Eng. Sci. 138 (2015) 239–243.
[10] Y. Zhong, P. Zhang, X. Zhu, H. Li, Q. Deng, J. Wang, Z. Zeng, J.-J. Zou, S. Deng, Highly efficient alkylation using hydrophobic sulfonic acid-functionalized biochar as a catalyst for synthesis of high-density biofuels, ACS Sus. Chem. Eng. 7 (2019) 14973–14981.
[11] J. Yang, N. Li, G. Li, W. Wang, A. Wang, X. Wang, Y. Cong, T. Zhang, Synthesis of renewable high-density fuels using cyclopentanone derived from lignocellulose, Chem. Comm. 50 (2014) 2572–2574.
[12] Y. Yang, Z. Du, Y. Huang, F. Lu, F. Wang, J. Gao, J. Xu, Conversion of furfural into cyclopentanone over Ni-Cu bimetallic catalysts, Green. Chem. 15 (2013) 1932–1940.
[13] Y. Liu, G. Li, Y. Hu, A. Wang, F. Lu, J.-J. Zou, Y. Cong, N. Li, T. Zhang, Integrated conversion of cellulose to high-density aviation fuel, Joule 3 (2019) 1028–1036.
[14] C. Zhao, D.M. Camaioni, J.A. Lercher, Selective catalytic hydroalkylation and deoxygenation of substituted phenols to bicycloalkanes, J. Catal. 288 (2012) 92–103.
[15] Q. Deng, G. Nie, L. Pan, J.-J. Zou, X. Zhang, L. Wang, Highly selective self-condensation of cyclic ketones using MOF-encapsulating phosphotungstic acid for renewable high-density fuel, Green. Chem. 17 (2015) 4473–4481.
[16] D. Lorenzo, A. Santos, E. Simón, A. Romero, Kinetics of alkali-catalyzed condensation of impurities in the cyclohexanone purification process, Ind. Eng. Chem. Res. 52 (2013) 2257–2265.
[17] Z. Wang, J.M. Heising, A. Clearfield, Sulfonated microporous organic-inorganic hybrids as strong Bronsted acids, J. Am. Chem. Soc. 125 (2003) 10375–10383.
[18] Y. Jing, Y. Xin, Y. Guo, X. Liu, Y. Wang, Highly efficient Nb_2O_5 catalyst for aldol condensation of biomass-derived carbonyl molecules to fuel precursors, Chin. J. Catal. 40 (2019) 1168–1177.
[19] D.T. Ngo, Q. Tan, B. Wang, D.E. Resasco, Aldol condensation of cyclopentanone on hydrophobized MgO. promotional role of water and changes in the rate-limiting step upon organosilane functionalization, ACS Catal. 9 (2019) 2831–2841.
[20] Y.S. Mahajan, R.S. Kamath, P.S. Kumbhar, S.M. Mahajani, Self-condensation of cyclohexanone over ion exchange resin catalysts: kinetics and selectivity aspects, Ind. Eng. Chem. Res. 47 (2008) 25–33.
[21] C. Pei, J. Gong, Tandem catalysis at nanoscale, Science 371 (2021) 1203–1204.
[22] S. Liu, P.A. Kots, B.C. Vance, A. Danielson, D.G. Vlachos, Plastic waste to fuels by hydrocracking at mild conditions, Sci. Adv. 7 (2021) eabf8283.
[23] J. He, Z. Wu, Q. Gu, Y. Liu, S. Chu, S. Chen, Y. Zhang, B. Yang, T. Chen, A. Wang, B. M. Weckhuysen, T. Zhang, W. Luo, Zeolite-tailored active site proximity for the efficient production of pentanoic biofuels, Angew. Chem. Int. Ed. 60 (2021) 23713–23721.
[24] M. Choi, Z. Wu, E. Iglesia, Mercaptosilane-assisted synthesis of metal clusters within zeolites and catalytic consequences of encapsulation, J. Am. Chem. Soc. 132 (2010) 9129–9137.
[25] Q. Sun, N. Wang, T. Zhang, R. Bai, J. Yu, Zeolite-encaged single-atom rhodium catalysts: highly-efficient hydrogen generation and shape-selective tandem hydrogenation of nitroarenes, Angew. Chem. Int. Ed. 58 (2019) 18570–18576.
[26] W. Ning, Q. Sun, R. Bai, X. Li, G. Guo, J. Yu, In situ confinement of ultrasmall Pd clusters within nanosized silicalite-1 zeolite for highly efficient catalysis of hydrogen generation, J. Am. Chem. Soc. 138 (2016) 7484–7487.
[27] Q. Sun, B.W.J. Chen, N. Wang, Q. He, A. Chang, C.-M. Yang, H. Asakura, T. Tanaka, M.J. Hulsey, C.-H. Wang, J. Yu, N. Yan, Zeolite-encaged Pd-Mn nanocatalysts for CO_2 hydrogenation and formic acid dehydrogenation, Angew. Chem. Int. Ed. 59 (2020) 20183–20191.
[28] Z. Wu, S. Goel, M. Choi, E. Iglesia, Hydrothermal synthesis of LTA-encapsulated metal clusters and consequences for catalyst stability, reactivity, and selectivity, J. Catal. 311 (2014) 458–468.
[29] J. Zhang, L. Wang, B. Zhang, H. Zhao, U. Kolb, Y. Zhu, L. Liu, Y. Han, G. Wang, C. Wang, D.S. Su, B.C. Gates, F.-S. Xiao, Sinter-resistant metal nanoparticle catalysts achieved by immobilization within zeolite crystals via seed-directed growth, Nat. Catal. 1 (2018) 540–546.
[30] L. Liu, U. Díaz, R. Arenal, G. Agostini, P. Concepción, A, Corma, Generation of subnanometric platinum with high stability during transformation of a 2D zeolite into 3D, Nat. Mater. 16 (2017) 132–138.
[31] Z. Jin, L. Wang, E. Zuidema, K. Mondal, M. Zhang, J. Zhang, C. Wang, X. Meng, H. Yang, C. Mesters, F.-S. Xiao, Hydrophobic zeolite modification for in situ peroxide formation in methane oxidation to methanol, Science 367 (2020) 193–197.
[32] C. Wang, W. Liang, Z. Jian, W. Hong, J.P. Lewis, F.S. Xiao, Product selectivity controlled by zeolite crystals in biomass hydrogenation over a palladium catalyst, J. Am. Chem. Soc. 138 (2016) 7880–7888.
[33] C. Wang, Z. Liu, L. Wang, X. Dong, J. Zhang, G. Wang, S. Han, X. Meng, A. Zheng, F.S. Xiao, Importance of zeolite wettability for selective hydrogenation of furfural over Pd@zeolite catalysts, ACS Catal. 8 (2018) 474–481.
[34] H.J. Cho, D. Kim, J. Li, D. Su, B. Xu, Zeolite-encapsulated Pt nanoparticles for tandem catalysis, J. Am. Chem. Soc. 140 (2018) 13514–13520.
[35] J.C. Hong, D. Kim, B. Xu, Selectivity control in tandem catalytic furfural upgrading on zeolite-encapsulated Pt nanoparticles through site and solvent engineering, ACS Catal. 10 (2020) 4770–4779.
[36] H. Cho, D. Kim, S. Li, D. Su, B. Xu, Molecular-level proximity of metal and acid sites in zeolite-encapsulated Pt nanoparticles for selective multistep tandem catalysis, ACS Catal. 10 (2019) 3340–3348.
[37] J.C. Hong, D. Kim, B. Xu, Pore size engineering enabled selectivity control in tandem catalytic upgrading of cyclopentanone on zeolite-encapsulated Pt nanoparticles, ACS Catal. 10 (2020) 8850–8859.

[38] C. Peng, J. Liang, H. Peng, R. Yan, W. Liu, Z. Wang, P. Wu, X. Wang, Design and synthesis of Cu/ZSM-5 catalyst via a facile one-pot dual-template strategy with controllable Cu content for removal of NO_x, Ind. Eng. Chem. Res. 57 (2018) 14967–14976.
[39] M. Gurrath, T. Kuretzky, H.P. Boehm, L.B. Okhlopkova, A.S. Lisitsyn, V. A. Likholobov, Palladium catalysts on activated carbon supports: influence of reduction temperature, origin of the support and pretreatments of the carbon surface, Carbon 38 (2000) 1241–1255.
[40] H. Xiong, Z. Liu, X. Chen, H. Wang, W. Qian, C. Zhang, A. Zheng, F. Wei, In situ imaging of the sorption-induced subcelltopological flexibility of a rigid zeolite framework, Science 376 (2022) 491–496.
[41] J. Zhong, D. Bin, Y. Feng, K. Zhang, J. Wang, C. Wang, J. Guo, P. Yang, Y. Du, Synthesis and high electrocatalytic activity of Au-decorated Pd heterogeneous nanocube catalysts for ethanol electro-oxidation in alkaline media, Catal. Sci. Technol. 6 (2016) 5397–5404.
[42] Q. Deng, R. Gao, X. Li, J. Wang, Z. Zeng, J.-J. Zou, S. Deng, Hydrogenative ring-rearrangement of biobased furanic aldehydes to cyclopentanone compounds over Pd/pyrochlore by introducing oxygen vacancies, ACS Catal. 10 (2020) 7355–7366.
[43] C. Liu, J. Liu, S. Yang, C. Cao, W. Song, Palladium nanoparticles encapsulated in a silicalite-1 zeolite shell for size-selective catalysis in liquid-phase solution, ChemCatChem 8 (2016) 1279–1282.
[44] Y. Liu, W. Qiang, T. Ji, M. Zhang, M. Li, J. Lu, Y. Liu, Uniform hierarchical MFI nanosheets prepared via anisotropic etching for solution-based sub-100-nm-thick oriented MFI layer fabrication, Sci. Adv. 6 (2020) 5993.
[45] T. Lida, D. Zanchet, K. Ohara, T. Wakihara, Y. Román-Leshkov, Concerted bimetallic nanocluster synthesis and encapsulation via induced zeolite framework demetallation for shape and substrate selective heterogeneous catalysis, Angew. Chem. Int. Ed. 57 (2018) 6454–6458.
[46] M. Zhang, L. Liu, L. Wang, X. Zhang, G. Li, Four-carbon segmented discrete hydrocracking of long-chain paraffins in MTT channels following a pore-mouth mechanism, ACS Catal. 12 (2022) 10313–10325.
[47] Q. Deng, X. Zhang, W. Li, J.J. Zou, Catalytic isomerization and oligomerization of endo-dicyclopentadiene using alkali-treated hierarchical porous HZSM-5, Chem. Eng. Sci. 135 (2015) 540–546.
[48] Z. Liu, J. Yuan, J.M. van Baten, J. Zhou, X. Tang, C. Zhao, W. Chen, X. Yi, R. Krishna, G. Sastre, A. Zheng, Synergistically enhance confined diffusion by continuum intersecting channels in zeolites, Sci. Adv. 7 (2021) 0775.
[49] R. Wang, G. Li, H. Tang, A. Wang, G. Xu, Y. Cong, X. Wang, T. Zhang, N. Li, Synthesis of decaline-type thermal-stable jet fuel additives with cycloketones, ACS Sus. Chem. Eng. 7 (2019) 17354–17361.
[50] S. Shao, W. Dong, X. Li, H. Zhang, R. Xiao, Y. Cai, Solvent-free synthesis of jet fuel by aldol condensation and hydroprocessing of cyclopentanone as biomass-derivates, J. Clean. Prod. 250 (2020), 119459.
[51] W. Wang, X. Zhang, Z. Jiang, Y. Cui, Q. Kang, X. Zhao, Q. Zhang, L. Ma, Controllably produce renewable jet fuel with high-density and low-freezing points from lignocellulose-derived cyclopentanone, Fuel 321 (2022), 124114.
[52] A.J. Kumalaputri, C. Randolph, E. Otten, H.J. Heeres, P.J. Deuss, Lewis acid catalyzed conversion of 5-hydroxymethylfurfural to 1,2,4-benzenetriol, an overlooked biobased compound, ACS Sus. Chem. Eng. 6 (2018) 3419–3425.
[53] Z.D. Young, S. Hanspal, R.J. Davis, Aldol condensation of acetaldehyde over titania, hydroxyapatite, and magnesia, ACS Catal. 6 (2016) 3193–3202.
[54] D.T. Ngo, Q. Tan, B. Wang, D.E. Resasco, Aldol condensation of cyclopentanone on hydrophobized MgO. Promotional role of water and changes in the rate-limiting step upon organosilane functionalization, ACS Catal. 9 (2019) 2831–2841.
[55] S. Bhasker-Ranganath, M.S. Rahman, C. Zhao, F. Calaza, Z. Wu, Y. Xu, Elucidating the mechanism of ambient-temperature aldol condensation of acetaldehyde on ceria, ACS Catal. 11 (2021) 8621–8634.
[56] M. Chen, N. Maeda, A. Baiker, J. Huang, Hydrogenation of acetophenone on Pd/silica-alumina catalysts with tunable acidity: mechanistic insight by in situ ATR-IR spectroscopy, ACS Catal. 8 (2018) 6594–6600.
[57] Q. Deng, X. Hou, Y. Zhong, J. Zhu, J. Wang, J. Cai, Z. Zeng, J.-J. Zou, S. Deng, T. Yoskamtorn, S.C.E. Tsang, 2D MOF with compact catalytic sites for the one-pot synthesis of 2,5-dimethylfuran from saccharides via tandem catalysis, Angew. Chem. Int. Ed. 61 (2022), e202205453.
[58] Z. Jin, X. Yi, L. Wang, S. Xu, C. Wang, Q. Wu, L. Wang, A. Zheng, F.-S. Xiao, Metal-acid interfaces enveloped in zeolite crystals for cascade biomass hydrodeoxygenation, Appl. Catal. B: Environ. 254 (2019) 560–568.